Experimentally informed micromechanical modelling of cement paste
An approach coupling X-ray computed tomography and statistical nanoindentation

Zhang, Hongzhi; Šavija, Branko; Luković, Mladena; Schlangen, Erik

DOI
10.1016/j.compositesb.2018.08.102

Publication date
2019

Document Version
Final published version

Published in
Composites Part B: Engineering

Citation (APA)
Zhang, H., Šavija, B., Luković, M., & Schlangen, E. (2019). Experimentally informed micromechanical modelling of cement paste: An approach coupling X-ray computed tomography and statistical nanoindentation. *Composites Part B: Engineering*, *157*, 109-122. https://doi.org/10.1016/j.compositesb.2018.08.102

Composites Part B 157 (2019) 109–122

Contents lists available at ScienceDirect

Composites Part B

journal homepage: www.elsevier.com/locate/compositesb

Experimentally informed micromechanical modelling of cement paste: An approach coupling X-ray computed tomography and statistical nanoindentation

Hongzhi Zhang*, Branko Šavija, Mladena Luković, Erik Schlangen

Faculty of Civil Engineering and Geosciences, Delft University of Technology, 2628 CN, Delft, the Netherlands

A B S T R A C T

This work proposes a method for numerically investigating the fracture mechanism of cement paste at the microscale based on X-ray computed tomography and nanoindentation. For this purpose, greyscale level based digital microstructure was generated by X-ray microcomputed tomography with a resolution of 2 μm/voxel length. In addition, statistics based micromechanical properties (*i.e.* Young's modulus and hardness) were derived from the grid nanoindentation test which was set to have an interaction volume the same as the resolution of the digital microstructure. A linear relationship between the two probability density functions of greyscale level and local Young's modulus was assumed and verified by the two-sample Kolmogorov-Smirnov (K–S) statistic. Based on this assumption, the fracture and deformation of a digital cubic volume with a dimension of 100 μm under uniaxial tension was simulated using a lattice fracture model. In addition, the influence of heterogeneity on fracture response was studied. Furthermore, the proposed method was compared with the results obtained from a traditional approach used previously by the authors in which discrete phases (capillary pore, anhydrous cement clinker, outer and inner hydration products) were considered. The two methods show similar crack patterns and stress-strain responses. The proposed method is regarded more promising as it captures also the gradient of material properties (within the discrete phases) in the cement paste.

1. Introduction

Cement paste is the main binding phase in concrete. As such, its mechanical properties are of great importance for the properties of this composite material. Therefore, prediction of concrete performance depends to a large extent on good understanding of cement paste behaviour. For predicting its mechanical properties, it is common to use micromechanical models. Micromechanical modelling of cement paste has generated considerable research interest recently as it provides an insight into the link between the material's microstructure and its global functional performance. In order to simulate the fracture behaviour of cement paste, the microstructure and micromechanical properties of its constituents need to be characterised.

Cement paste is a multi-phase material comprising several phases, most importantly calcium silicate hydrate (C–S–H), calcium hydroxide (CH), anhydrous cement clinker and pores. Consequently, micromechanical models consider, in general, a multi-phase microstructure. This microstructure can be obtained either by numerical modelling [1–3] or experiments [4–7]. Both of these approaches rely heavily on the theoretical knowledge of the microstructure evolution of the material. Compared with the experiments, numerical cement hydration models have clear advantages in terms of time effort and ease of use. In such models cement clinkers are commonly modelled as spheres [1,2]. This simplification, however, has an influence on the simulated hydration of cement [8]. Cement hydration models that consider realistic particle shapes are still rare [3,9]. Regarding with the elasticity estimation, the simulated microstructure has a strong influence on early-age [10]. Although the microstructure has less influence in the later hydration stage, where phase volume fractions dominate the elasticity, it plays a key role in determining the material strength [11]. On the other hand, X-ray computed tomography (XCT) is becoming a general technique for three-dimensional microstructure characterisation of cement-based materials [7,12–14]. X-ray computed tomography can visualise the spatial distribution of cement phases with different densities by greyscale levels. The phase segmentation can then be performed to identify the spatial distribution of distinct hydration phases. However, phase segmentation is not a standardized technique: many methods exist, and it is difficult, if not impossible, to ascertain which segmentation method produces more accurate results. For example, the identified pore phase volume varies significantly depending on the applied segmentation method. In the literature [15] and [16], XCT images with similar resolution are obtained. However, a tangent-slope method merely depending on the greyscale level histogram results in a lower calculated porosity (8.65% [15]) compared with the one from Ref. [16] using theoretical porosity from Power's model (30%) as criteria to conduct segmentation. Since this is only the first step in

* Corresponding author.
E-mail addresses: h.zhang-5@tudelft.nl (H. Zhang), b.savija@tudelft.nl (B. Šavija), m.lukovic@tudelft.nl (M. Luković), erik.schlangen@tudelft.nl (E. Schlangen).

https://doi.org/10.1016/j.compositesb.2018.08.102
Received 16 May 2018; Received in revised form 19 July 2018; Accepted 23 August 2018
Available online 27 August 2018
1359-8368/

micromechanical modelling, there is uncertainty already in the input. As the models are built up, there are additional sources of uncertainty, and it would be of great use to minimize the subjectivity involved in the thresholding procedure of the multi-phase material structure. To this end, this article tries to address the following question: *can we avoid thresholding and use directly the greyscale material structure obtained from X-ray computed tomography as input for the micromechanical modelling of cement paste?*

Another important aspect for the micromechanical modelling of cement paste are the micromechanical properties of local hydration phases. These micromechanical properties can be measured by statistical nanoindentation [17–20] or calculated using molecular dynamics simulations [21,22]. At the moment, it is difficult to directly use the data from these simulations as the real crystalline structures in cement paste are more complex compared with the ideal situation. Furthermore, the input mechanical properties are resolution-dependent for the discrete micromechanics models [23]. This is because the material components and their relative amounts within the voxel (3-dimensional pixel) vary with the resolution. In the statistical nanoindentation test, a large number of indentation tests are performed in a grid without prior knowledge of the microstructure of the probed microvolume - generally termed the interaction volume [17]. The micromechanical properties (stiffness and hardness) of individual phases (anhydrous cement clinkers, low- and high-density hydration products) are extracted by analysing the histograms with statistical methods such as the deconvolution method [17,24,25]. These values are widely used as input to perform micromechanical simulations [15,16,18,26–30]. However, it should be noted that the scatter in the results is big and it is debated in literature whether this method can be used at all for heterogeneous materials like cement paste [24,25,31–33]. A reason for this is that, although the tip-radius is very small (in case of the typically used Berkovich tip), it is almost impossible to probe a single phase; in fact, a composite made up of different phases is probed by indenting the material with a diamond tip [25]. Furthermore, when dealing with cement paste, which is a 3D heterogeneous material, the indentation outcome is always influenced by the underlying material, which can be stiffer and harder or just the opposite [33]. On the other hand, a question always arsing is how many phases should be considered in the modelling as it is still debated whether two clearly distinct phases with distinct mass densities exist [18,34–37]. Therefore, the following question is addressed: *can we avoid deconvolution or averaging and use directly the micromechanical properties obtained from nanoindentation as input for the micromechanical modelling of cement paste?*

This work proposes a new method for micromechanical simulations of cement paste based on a combination of statistical nanoindentation and XCT technique without the need for explicit identification of distinct phases. The material structure of cement paste was characterised by XCT and corresponding histogram of grey scale distribution. The probability density function (PDF) of micromechanical properties (i.e. histogram of micromechanical properties) was quantified using statistical nanoindentation. Without image segmentation or histogram deconvolution, micromechanical properties were directly correlated with the greyscale level by a linear equation. The linear relationship assumption was further verified by two-sample Kolmogorov-Smirnov (K−S) statistics. The influence of heterogeneity on fracture and deformation behaviour was studied by randomizing the “realistic” microstructure. Furthermore, the newly developed approach has been compared to the method considering distinct phases, previously used by the authors. Strengths and drawbacks of both methods are compared and discussed.

2. Experimental

2.1. Materials

The tested material was a standard grade OPC CEM I 42.5 N paste with 0.4 water-to-cement ratio. First, cement was mechanically mixed with deionized water and cast into a PVA cylinder mould (diameter 24 mm, height 39 mm). After 28 days hydration, the sample was demoulded and cut into discs with thickness of 2 mm using a diamond saw. Solvent exchange method using isopropanol was used to stop hydration of cement paste [38]. The middle portion of the slices was cut out to prepare the specimens for nanoindentation test.

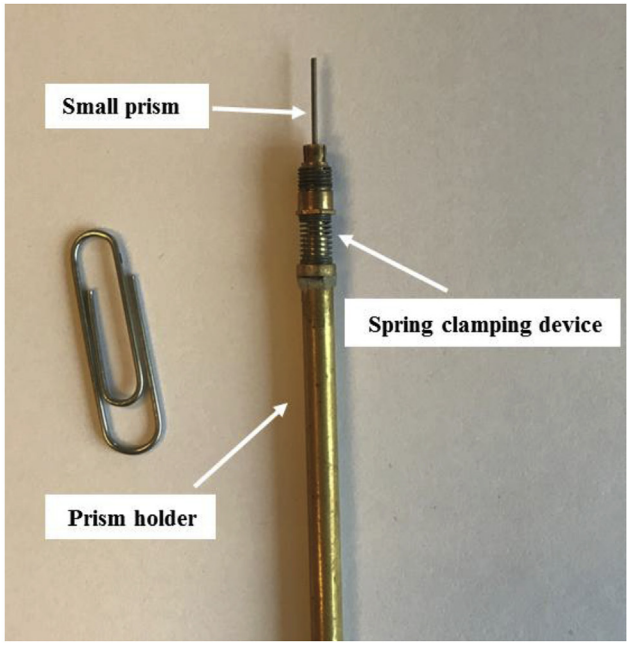

(a)

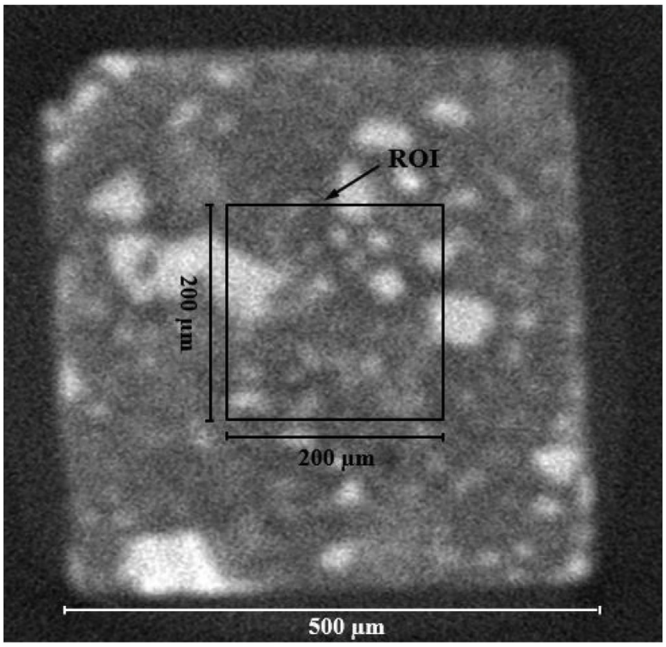

(b)

Fig. 1. Schematic view of XCT experiment: **(a)** small prism clamped on the special holder for CT scanning, after [23]; **(b)** an example cross sectional XCT image of ROI.

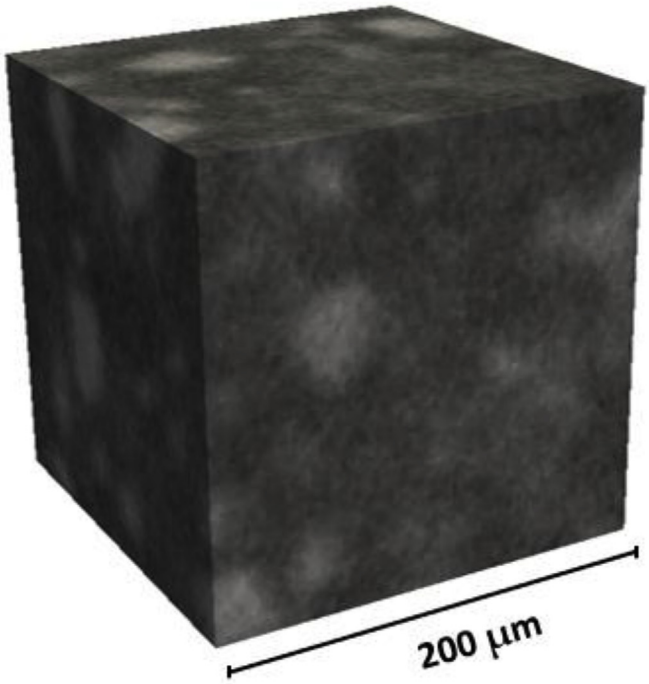

(a)

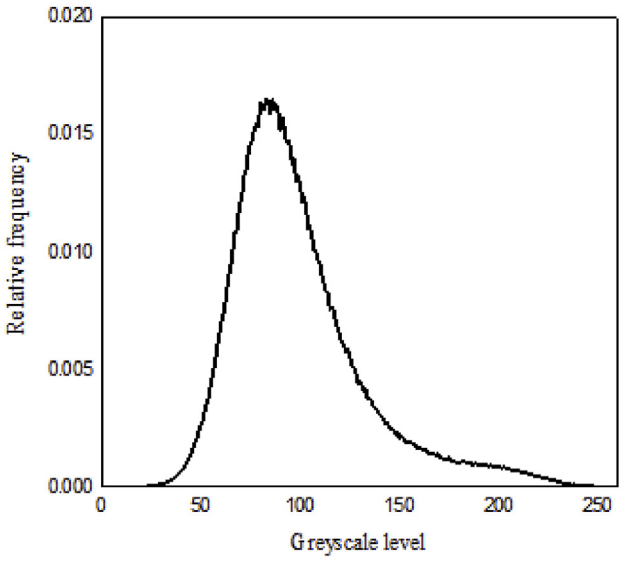

(b)

Fig. 2. Results of XCT: **(a)** a cubic volume of a reconstructed 3D microstructure; **(b)** histogram of greyscale level distribution of a volume having 10^6 voxels (8×10^6 µm^3).

2.2. XCT scanning

For acquiring greyscale based digital material structure, a small cement paste prism with cubic cross-section of 500 µm × 500 µm and length of 2 mm was produced by grinding, polishing and micro-dicing, and scanned by a Micro CT-Scanner (Phoenix Nanotom, Boston, MA, USA). The readers are referred to [23,39] for more details about the specimen preparation procedure. Fig. 1a shows the small prism fixed in a special holder that can be clamped by the rotatable stage of the CT-scanner. The X-ray source tube was set as 120 kev/60 µA during scanning. 2800 images with an exposure of 6 s were acquired on a digital GE DXR detector (3072 × 2400 pixels). The voxel resolution under these conditions was 2 × 2 × 2 µm^3/voxel. Reconstructed slices were carried out with Phoenix Datos|x software and a 3D stack of 8-bit cross-section images were generated in the end. A cubic region of interest (ROI) with a length of 200 µm was extracted from the specimen for the statistical analysis (See Fig. 1b). To diminish the influence of beam hardening in the XCT experiment, the middle region of the specimen was chosen and analysed.

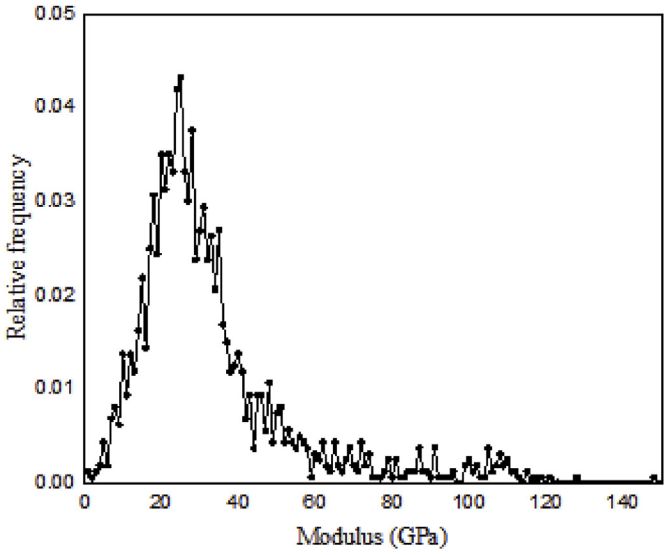

Fig. 3. Histogram of Young's modulus from nanoindentation experiments on cement paste.

2.3. Nanoindentation

Prior to nanoindentation, the samples were ground and polished to achieve a smooth surface. For purpose of grinding, sandpapers (180, 240, 400, 600 and 800 and 1200 grit) were used in order and each sandpaper was used for 5 min-10 min. Instead of water, ethanol was used as a cooling liquid to prevent further hydration of residual cement clinkers. After grinding, samples were polished with diamond paste (6 µm, 3 µm, 1 µm, and 0.25 µm) on a lapping table in order and soaked into an ultrasonic bath to remove any residue between each polishing step. Sample preparation was performed just prior to testing to avoid carbonation of the tested surface.

An Agilent Nano Indenter G200 (Keysight, Santa Rosa, CA, USA) with a diamond Berkovich tip was used for nanoindentation tests. Quartz standard was indented before the test to ensure accuracy. Three specimens in total were tested. The indentation depth was 700 nm. For each specimen, a series of 25 × 20 indents were performed on a tightly spaced grid, with spacing of 20 µm between indents. This makes 1500 indents in total covering an area of 0.6 mm^2. The Continuous Stiffness Method (CSM) developed by Oliver and Pharr [40] was used. This method consists of superimposing a small oscillation on the primary loading signal and analysing the response of the system by means of a frequency-specific amplifier. As a consequence, it enables a continuous measure of contact stiffness as a function of indentation depth and not just at the point of initial unloading. Therefore, hardness and indentation modulus are obtained as a continuous function of surface penetration depth.

The nanoindentation measurements encompass mechanical properties of the local (indented) material microstructure but also the microstructure around the indent, generally with the length scale around

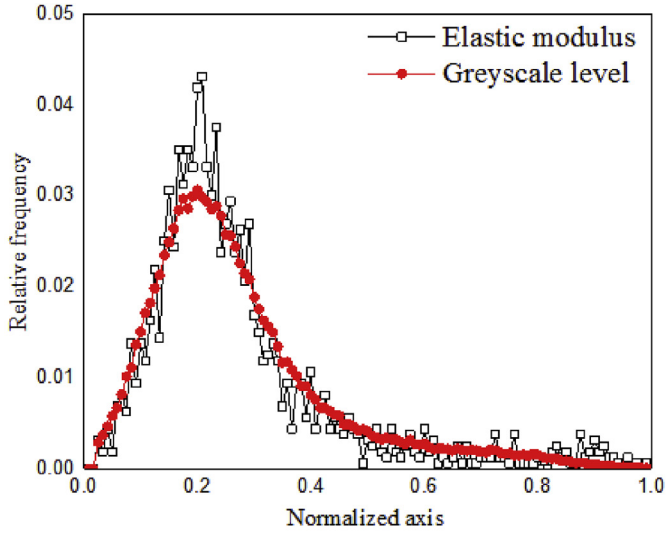

(a)

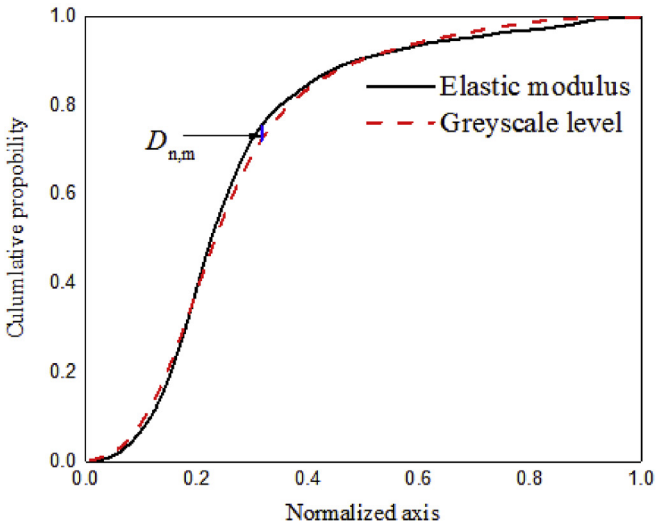

(b)

Fig. 4. Comparison of distributions of Young's modulus and greyscale level with normalized axis: **(a)** histogram of two distributions; **(b)** cumulative probability of two distributions.

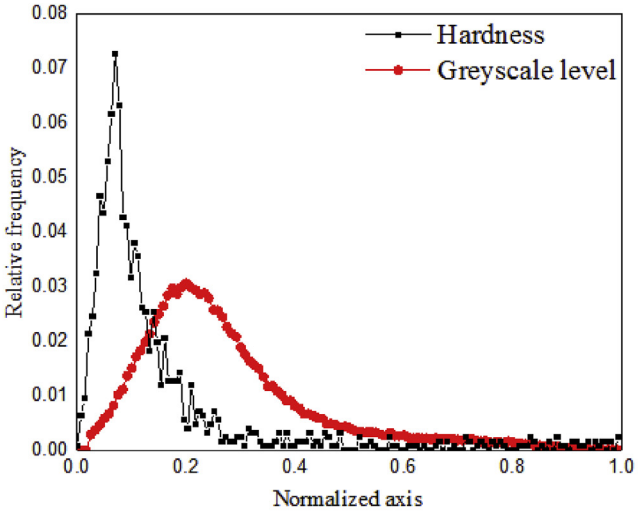

(a)

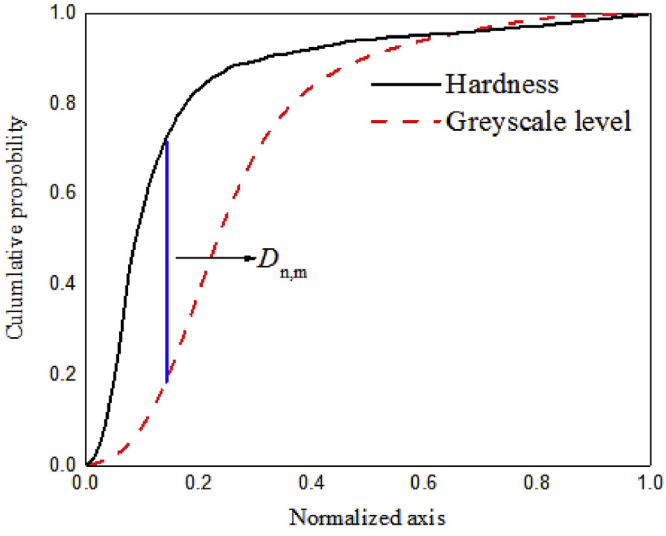

(b)

Fig. 6. Comparison of distributions of hardness and greyscale level with normalized axis: (a) histogram of two distributions; (b) cumulative probability of two distributions.

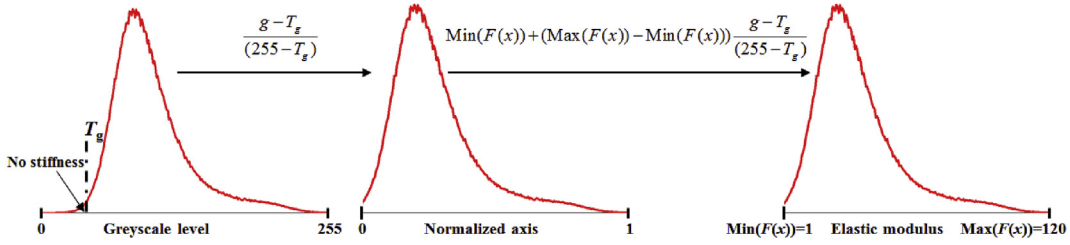

Fig. 5. A sketch of the interval conversion.

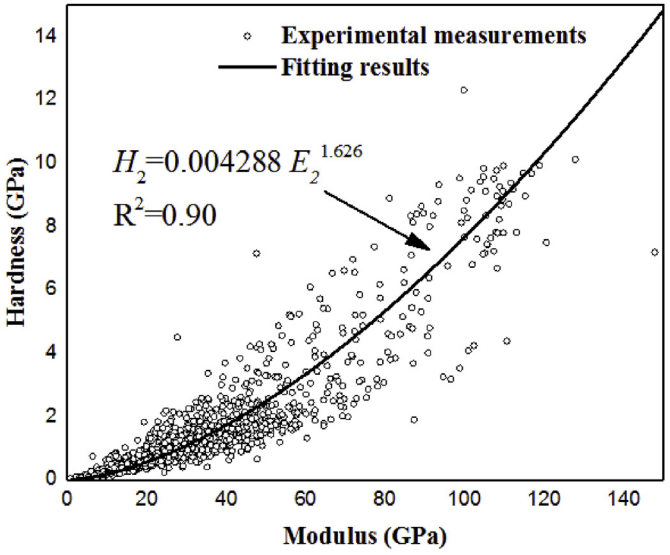

Fig. 7. Relationship between hardness and Young's modulus from nanoindentation.

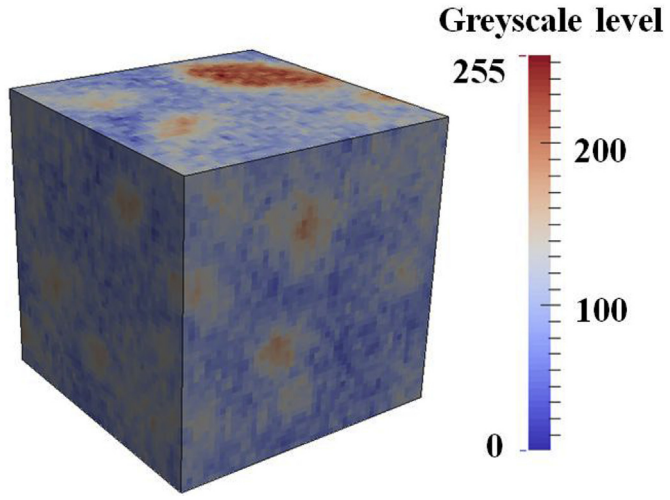

Fig. 8. A greyscale based digital material structure of cement paste with a cubic dimension of 100 μm × 100 μm × 100 μm.

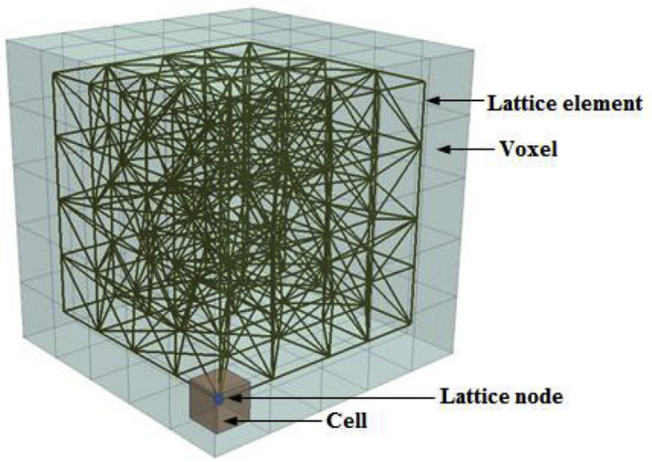

Fig. 9. Schematic view of lattice mesh construction of a cubic volume of 5 voxel × 5 voxel × 5 voxel.

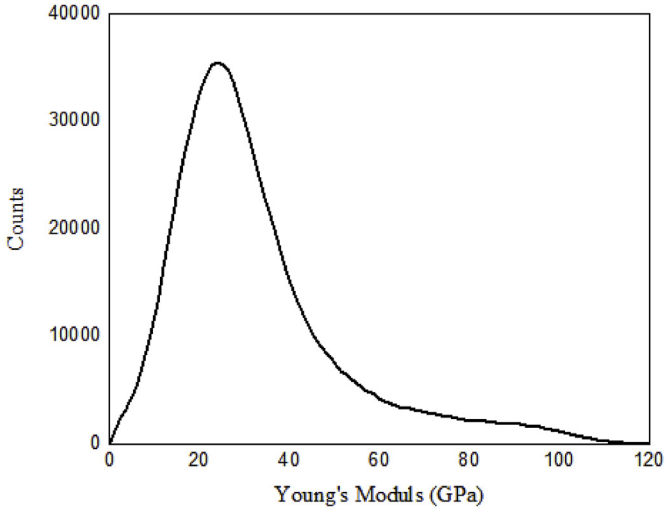

(a)

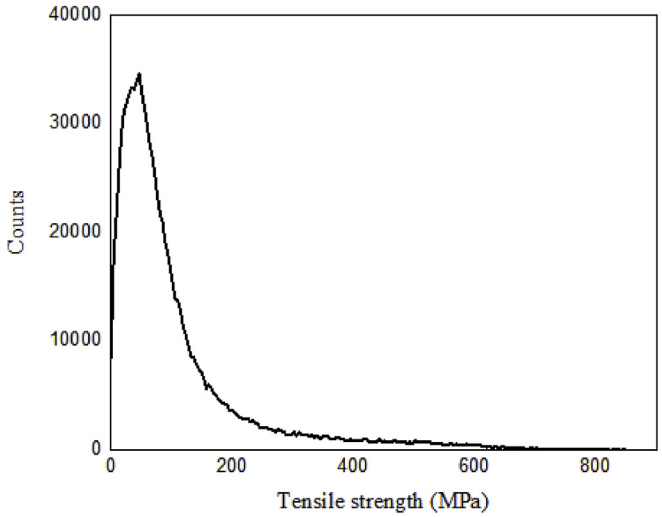

(b)

Fig. 10. Distribution of assigned mechanical properties of beam elements: **(a)** Young's modulus; **(b)** tensile strength.

3–5 h_{max}, where h_{max} is the maximum indentation depth [41,42]. This ratio between the indentation depth and interaction length (and volume) has been proposed in the literature [43–45], where correlation of micromechanical and chemical properties measured by nanoindentation and WDS measurements (wavelength dispersive spectroscopy) was performed. In order to compare the results from nanoindentation and CT scan, it was necessary to make the interaction volume the same as the voxel size in CT scan. Therefore, the average E modulus and hardness were determined in the displacement range between 400 nm and 660 nm. For the calculation, Poisson's ratio of the indented material was taken as 0.18 in the CSM method.

2.4. Experimental results and assumptions

As shown in Fig. 2a, the XCT provides visualization of the attenuation coefficients of material by greyscale level. Therefore, greyscale level of each individual voxel is determined by the attenuation coefficient of that voxel. It has been shown in the literature that the

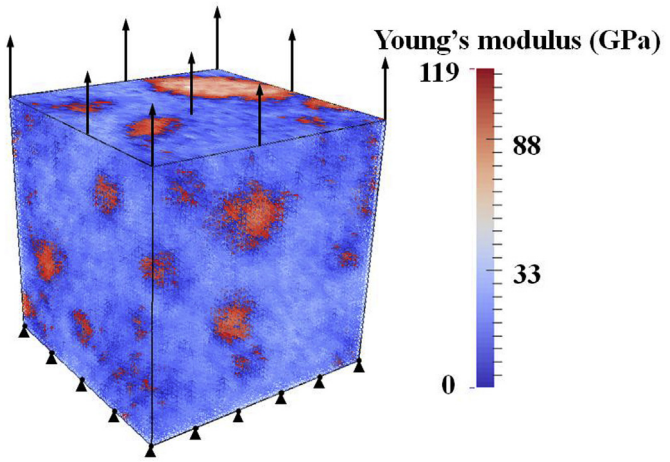

Fig. 11. Lattice system under uniaxial tension.

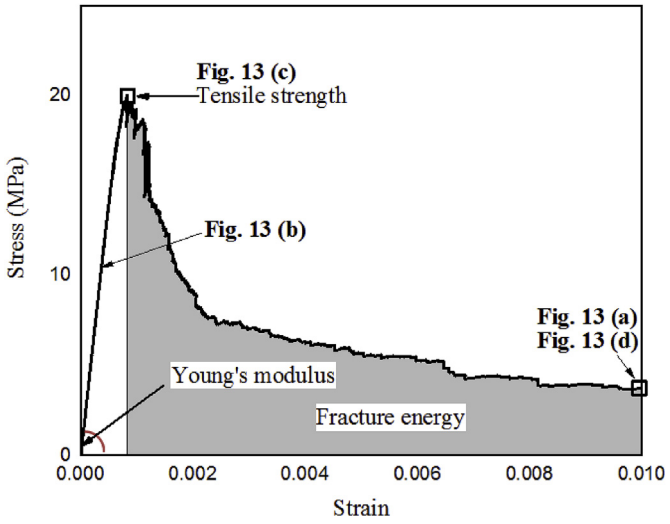

Fig. 12. Simulated stress-strain curve of cement paste under uniaxial tension test (points for which crack patterns are displayed are marked).

Table 1
Simulated micromechanical properties of Portland cement paste (w/c = 0.4), corresponding with Fig. 12.

Young's modulus (GPa)	Tensile strength (MPa)	Strain at peak load (%)	Fracture energy (J/m^2)
28.53	20.01	0.08	5.89

grey scale value can be correlated to the density and atomic number of the material [46]. For a constant applied voltage of the X-ray tube, there is a linear relationship between the greyscale level and the material density [47]. By virtue of this relationship, X-ray tomography can be used to measure local density variations within the material given proper calibration [48–50]. However, due to the complex material structure of cement paste, purely analytical solution mapping the attenuation to physical density has not been achieved to date. Still, greyscale level map can be assumed to represent the density distribution [6,7,15]. In this case, the reconstructed image is coded on 8-bit (0–255) greyscale level. Value 0 is black corresponding to minimum density. Value 255 is white corresponding to maximum density. A greyscale level histogram of a volume with 200 μm × 200 μm × 200 μm (100 voxel × 100 voxel × 100 voxel) is shown in Fig. 2b, which is expected statistically representative for cement paste at this scale. Note that this does not mean that this is a representative volume element (RVE) of cement paste. If an RVE exist depends on the process that is being considered, for fracture of softening materials an RVE might not exist due to localization issues [51].

Similar to the greyscale level, there is a relation between density and mechanical properties [52]. Therefore, an attempt is made here to correlate two values that are both density dependent: greyscale level obtained from XCT, and micromechanical properties of cement paste. With respect to bone material, elastic modulus can be linked to the CT number for the finite element model [53–55]. The CT number is represented by the Hounsfield unit and has a linear relationship with the greyscale level [56]. For cement-based materials, no published data was found defining this relationship because of the complex material structure. As the main aim of this study is to show the possibility of using a continuous model for micromechanical modelling of cement paste, a simple linear relationship between the greyscale level and elastic modulus was assumed. Nevertheless, this relationship has to be validated before it can be used as input for the modelling. The distribution of the local Young's modulus and hardness are plotted in Fig. 3 with a bin size of 1 GPa from 0 to 120 GPa. To test this approach, a two-sample Kolmogorov-Smirnov (K–S) test was performed. The K–S test is a non-parametric test, which quantifies the distance between the cumulative distribution functions of two samples [57,58]. The null hypothesis of K–S test generally sets as that the samples are drawn from the same distribution. For two given one-dimensional PDFs, the K–S statistic is:

$$D_{n,m} = \sup |F_{1,n}(x) - F_{2,m}(x)| \tag{1}$$

where $F_{1,n}$ and $F_{2,m}$ are the empirical distribution functions of the first and second sample respectively, and *sup* is the supremum function. The null hypothesis is rejected at level α if

$$D_{n,m} > c(\alpha)\sqrt{\frac{n+m}{nm}} \tag{2}$$

where n and m are the sizes of first and second sample respectively. In general, the value of c(α) is given by Ref. [59]:

$$c(\alpha) = \sqrt{-\frac{1}{2}\ln\left(\frac{\alpha}{2}\right)} \tag{3}$$

As shown in Fig. 4a, the two PDFs are linearly normalized to the range of 0–1 with a bin size of 0.01 and their cumulative probability functions are plotted in Fig. 4b. Commonly, with respect to a porous material, its stiffness approaches zero before its porosity equals 1 and a critical porosity (< 100%) always exists to represent the porosity leading to the zero stiffness [60]. In the XCT scan, voxels with porosity higher than the critical value *can* be detected (i.e. the air voxel with 100% porosity has a greyscale level equals 0.). However, a micro volume with zero stiffness *cannot* be tested by nanoindentation. Furthermore, a gap between the zero indentation modulus and minimum detected modulus between 1 and 2 GPa with a probability of 0.3% is also observed in the PDF of elastic modulus. Therefore, to make these two distributions comparable, voxels having undetectable indentation modulus have to be eliminated from the PDF of greyscale level. For this purpose, a greyscale level (at the left tail) having the same probability as the detectable stiffness was chosen as the threshold value (T_g = 42). Voxels having greyscale level lower than the threshold were then removed from the probability distribution measurements. This makes the initial greyscale level have the same probability as the minimum detected indentation modulus. Note that the probability of the minimum detected indentation modulus might change with the selected bin size. A bin size of 1 GPa was adopted herein.

In this case, $D_{n,m}$ is regarded as the maximum distance between the two cumulative probability curves which is calculated as 0.0348, and the c(α) is equal to 0.0351 with respect to a common level of α = 0.05 with m = 1500 and n = 125000 from Eq. (3). Therefore, it is concluded from the K–S test that the null hypothesis cannot be rejected indicating that the two samples are supposed to be drawn from the same

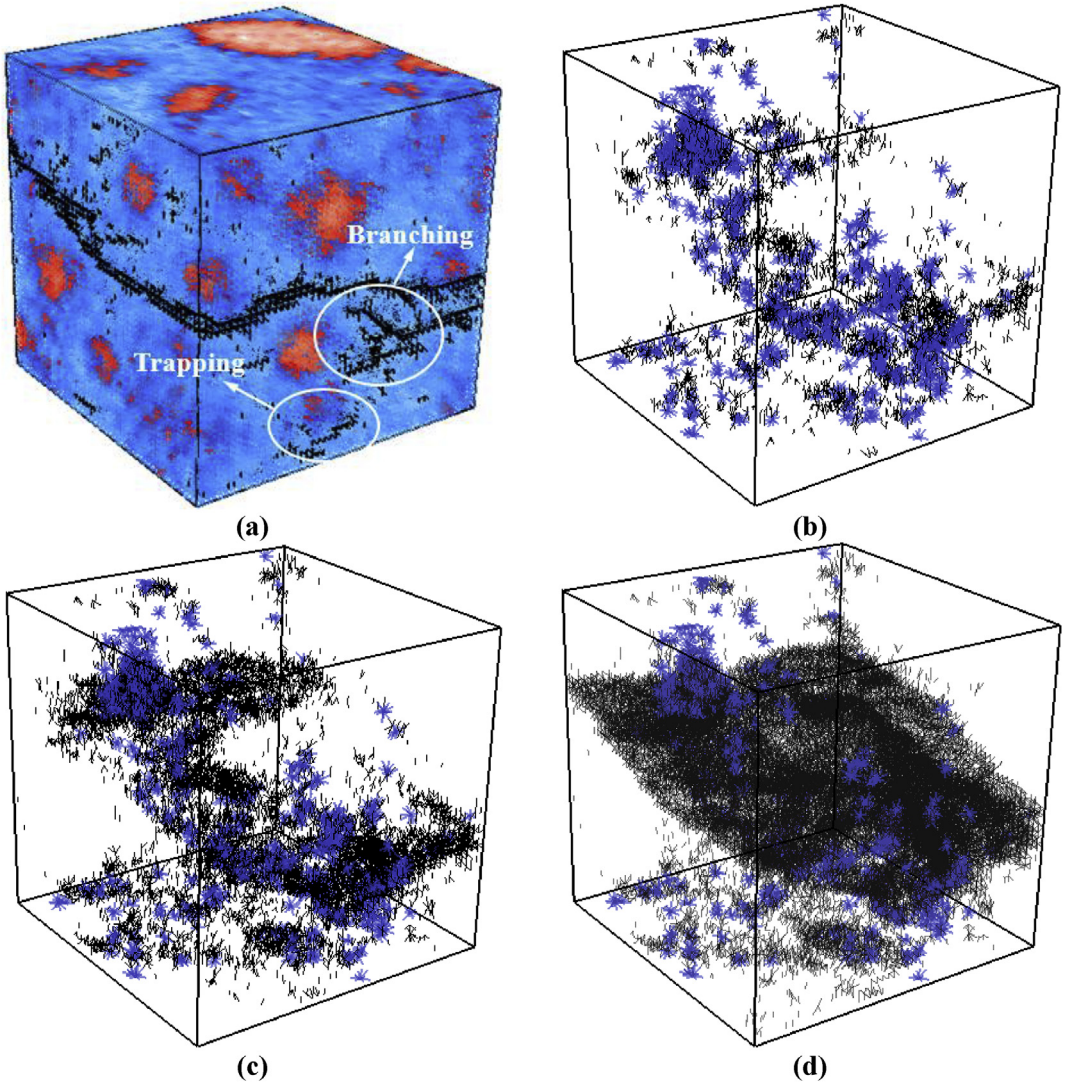

Fig. 13. Simulated fracture pattern of greyscale based microstructure: **(a)** deformed specimen with cracked elements at the final stage with a strain of 0.01; **(b)** crack pattern at elastic stage with 5000 elements cracked; **(c)** crack pattern at peak load with 14281 cracked elements; **(d)** crack pattern at the final stage with 53097 cracked elements (black represents cracked element; blue elements in the crack pattern represent elements having no strength/stiffness which are considered as the pre-existing defects in the simulation). (For interpretation of the references to colour in this figure legend, the reader is referred to the Web version of this article.)

distribution with a 95% confidence level. Therefore, for a specific greyscale level g of one voxel, its local Young's modulus can be addressed as:

$$E_{\text{local}} = \text{Min}(F(x)) + (\text{Max}(F(x)) - \text{Min}(F(x)))\frac{g - T_g}{(255 - T_g)} \quad (4)$$

where T_g is the greyscale that corresponds to the voxel having modulus equals to zero and equals 42 in this case. Min(F(x)) and Max(F(x)) are the minimum and maximum values that can be derived from Young's modulus histogram, and equal to 1 GPa and 120 GPa respectively. This procedure is schematically shown in Fig. 5.

Another parameter that obtained by nanoindentation is the microhardness which can be further linked to the ultimate tensile strength of the probed micro volume. The ratio between micro hardness and tensile strength varies between 3 to 183 for different materials [61]. For cement paste, this ratio is found to be around 12 by the authors [39]. In this study, micro-cubes of cement paste were created and split using a nanoindenter. Tensile strength of individual phases in the material was then determined through inverse analysis. Since hardness of cement phases is known, a ratio between hardness and tensile strength was then obtained. The PDF of measured hardness is plotted against the greyscale level as shown in Fig. 6a. The two-sample K−S statistics as descripted above shows a maximum distance: $D = 0.4392$ (Fig. 6b), which is greater than the critical value c(α) (0.0351) at the significance level: $\alpha = 0.05$. This indicates that the microhardness cannot be correlated with the greyscale level through a linear relation. In order to determine the microhardness, an empirical model in a form of power exponent ($H_{\text{local}} = aE_{\text{local}}{}^{b}$) is proposed to correlate the hardness with its corresponding Young's modulus and shows a good fit with a determination coefficient (R^2) of 0.90 (Fig. 7). Therefore, the local tensile strength can be determined as:

$$F_{local} = \frac{aE_{local}^{b}}{12} \quad (5)$$

where a and b are the empirical constants fitted from the experimental results. In this case, a = 0.004288 and b = 1.626. Relationships developed in this section are used in the micromechanical model as further described.

3. Modelling approach

For micromechanical modelling, a lattice-type model was used

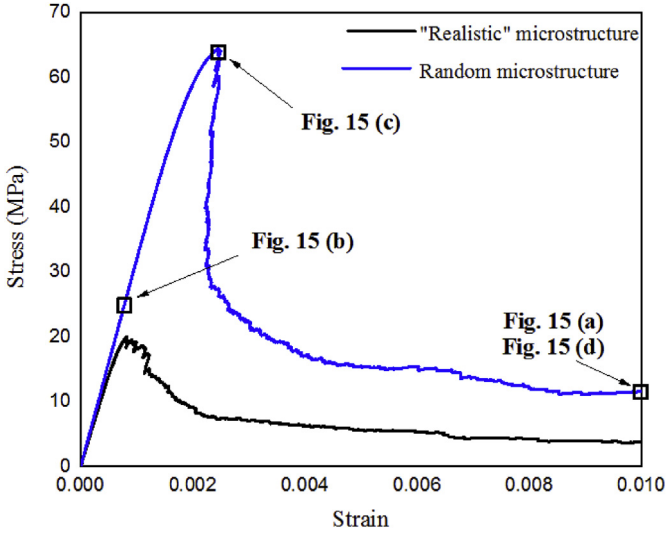

Fig. 14. Comparison of simulated stress-strain diagrams for realistic microstructure and randomized microstructure (points for which crack patterns are displayed are marked).

Table 2
Simulated micromechanical properties of randomized material structure.

Young's modulus (GPa)	Tensile strength (MPa)	Strain at peak load (%)	Fracture energy (J/m^2)
30.08	64.99	0.3	20.45

[62,63]. Lattice model is one of the most popular to simulate fracture in cement based-materials, mainly because the simulated cracks are very realistic and resemble to a great detail of the cracks observed in laboratory tests and in practice [64–66]. In this model, the material is discretised as a set of lattice beam elements. A set of linear analyses is then performed by calculating the response of the lattice mesh for a particular external displacement. The beam element with the highest stress-to-strength ratio is identified and removed from the lattice network. In each of the analysis steps, a single beam element is removed from the mesh, which represents the creation of a small crack, and causing a decrease in stiffness of the system. The analysis is repeated, with an updated mesh, until a pre-determined failure criterion is achieved. In addition, the material heterogeneity can be easily considered by overlaying a material structure to the lattice mesh. In the current study, the digitalized greyscale level based material structure was used. The modelling details are as follows:

First, a volume of cube with length of 100 μm (50 voxels) was randomly extracted from the greyscale images obtained by XCT (Fig. 8). The red colour represents the material with highest density, while blue denotes the lowest density. For each voxel, its corresponding Young's modulus and tensile strength were assigned according to its greyscale level (as described in section 2.4). For the simulations at this scale local brittle behaviour (a linear elastic, purely brittle constitutive law at beam level) is assumed. For the lattice modelling also a multi-scale modelling approach is developed and then local softening is used at higher scale levels [23,67].

Then a cell was defined within each voxel, as shown in Fig. 9. The nodes were then randomly positioned in each cell. A parameter is defined as the ratio between length of cell and voxel size to represent the randomness of the mesh. If the cell length -to-voxel ratio is equal to 0, there is no randomness, a node is then placed exactly in the centre of the voxel, and a regular mesh is created. If, on the other hand, the ratio is equal to 1, a node can be placed anywhere in the voxel, and a fully random mesh is created. Note that as the simulated crack shape is affected to a certain extent by the orientation of lattice elements, the simulated fracture behaviour of materials are somewhat affected by the choice of randomness [68]. In order to avoid large variations in length of elements and introduce geometry disorder of material texture, a randomness of 0.5 is generally adopted in the literature [39,63].

Delaunay triangulation was then performed on a set of nodes as described by Yip et al. [69], see Fig. 9. The mesh configuration that is chosen results in a Poisson's ratio of about 0.18 for the global performance, which is realistic for cementitious materials [70].

Elasticity modulus of beam element was ascribed as the harmonic average of the two connected voxels, while the tensile strength was assigned as the lower value of the two [71,72]. The elements connecting to the voxels with greyscale level lower than T_g (determined in section 2.4) were removed from the mesh as these voxels have undetectable indentation modulus. These removed elements represent the pre-existing defects in the system (see section 2.4). The distributions of input local mechanical properties are presented in Fig. 10.

After mapping micromechanical properties on the lattice mesh, a computational uniaxial tensile test was performed. Nodal displacement was imposed at one side while the deformation of nodes at the opposite side was completely restrained, see Fig. 11.

4. Numerical results and discussion

4.1. Results of proposed method

Fig. 12 shows simulated stress-strain curve from where Young's modulus (E), tensile strength (f_t) and fracture energy (G_f) can be calculated. The Young's modulus can be computed from the initial slope of the curve, while tensile strength corresponds to the peak point. Fracture energy was calculated from the post-peak part of the stress-strain curve as (Fig. 12):

$$G_f = \int_{u1}^{u2} \sigma du \tag{6}$$

where σ is the stress and u the displacement; u_1 corresponds to the displacement at peak load; u_2 denotes displacement at failure state and is regarded as 1 μm in this study. Note that the calculated fracture energy would be somewhat different if a different “cut-off” displacement was selected, but the main purpose of this work was to compare the fracture energy between different specimens. Herein, the simulated micromechanical properties are listed in Table 1. Such high strength of cement paste at microscale was recently experimentally measured by the authors [73]. In this work, 100 × 100 × 100 μm^3 cubes are produced and split using a wedge tip mounted on the nanoindenter. For cement paste with w/c = 0.4 (prepared in the same way and using the same materials as that used in the present study), the nominal splitting strength was found to be 18.72 MPa on average with a standard deviation of 3.85 MPa. The tensile strength at this scale is almost one order of magnitude lager than the value of laboratory centimetre sized samples. This is mainly attributed to the fact that the micro sized specimens are free from air voids or defects larger than the sample size which significantly decreases the macroscopic strength [74]. This trend has been shown by a material structure informed multi-scale fracture modelling [23]. Similar trend was observed in other quasi-brittle materials, e.g. nuclear graphite both experimentally [75] and numerically [67]. The value of Young's modulus obtained in the simulation (28.53 GPa) is in between the results reported by Lukovic et al. (around 33 GPa) [33] and Zhang et al. (25.4 GPa) [39], and close to the elastic resonance measurements (around 25 GPa) [76]. The difference between the results reported in the literature could be explained by the heterogeneity nature of such material which introduces the fluctuation of its micromechanical properties.

The deformed specimen in the final failure state is presented in Fig. 13a. The red elements represent material with relatively high modulus and strength, which can be regarded as the stiff inclusion in the structure (possibly anhydrous cement clinkers). It is clear that a

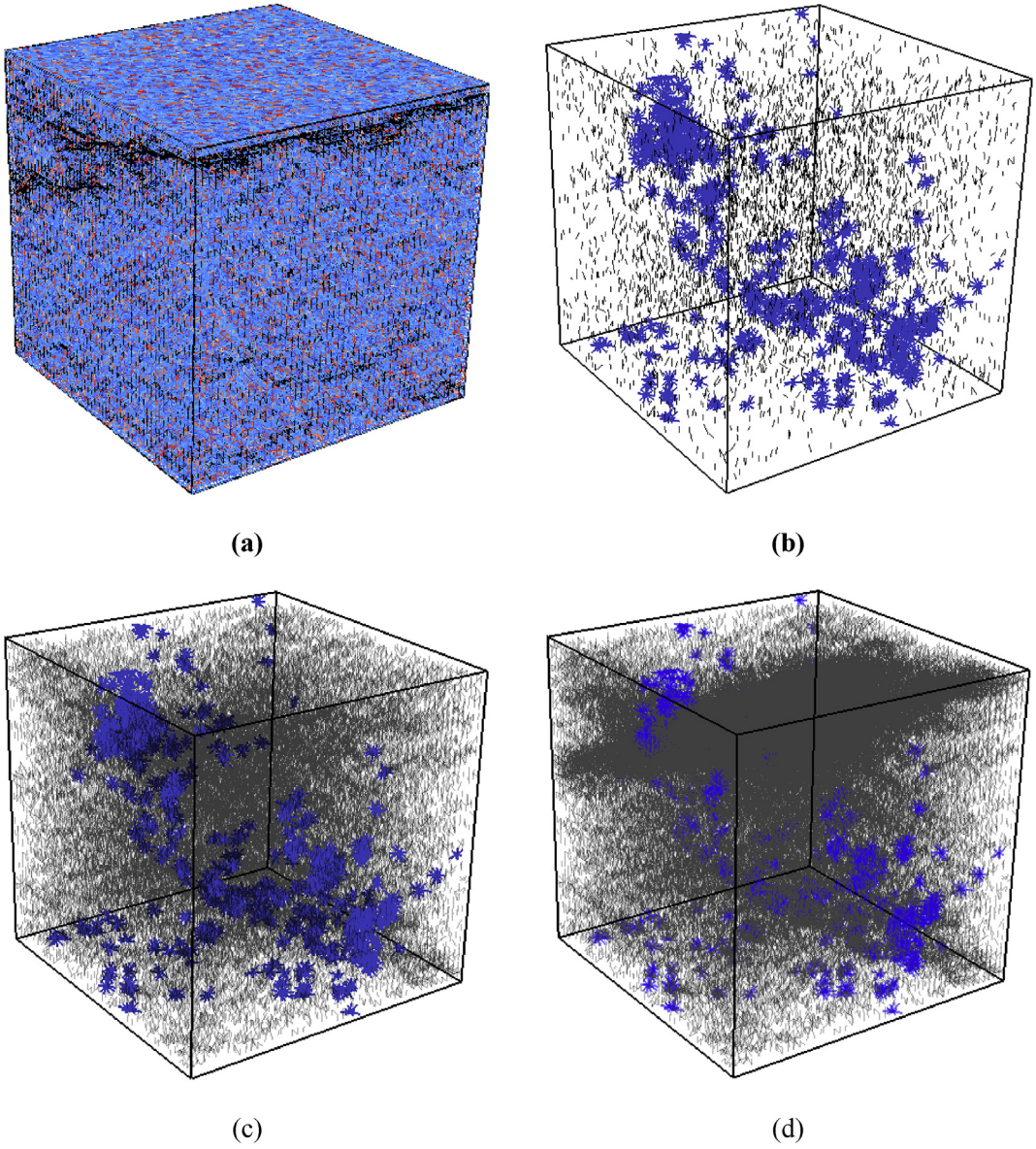

Fig. 15. Simulated fracture pattern of randomized microstructure: **(a)** deformed specimen with cracked elements at the final stage with a strain of 0.01; **(b)** crack pattern at initial stage with 5000 elements cracked; **(c)** crack pattern at peak load with 63677 cracked elements; **(d)** crack pattern at the final stage with 121464 cracked elements (black represents cracked element; blue elements in the crack pattern represent elements having no strength/stiffness which are considered as the pre-existing defects in the simulation). (For interpretation of the references to colour in this figure legend, the reader is referred to the Web version of this article.)

main crack disturbed by the stiff inclusion forms through the middle part of the volume. Similar behaviour was reported by Lukovic et al. [77]. Furthermore, crack branching and trapping are also observed. In order to have a clear look of the crack distribution and formation progress, the fracture patterns at certain failure stage are presented following. As shown in Fig. 13b, the distributed microcracks tend to initiate in the vicinity of the pre-existing defects where stress concentrations occur. After a certain level, the distributed micro cracks start localizing and nucleating and failure of the specimens follows (Fig. 13c). At the final stage (Fig. 13d), a main crack perpendicular to the loading direction is finally formed, leading to the failure of the test specimen.

4.2. Influence of heterogeneity

In order to investigate the influence of heterogeneity on the micromechanical performance of material structure, micromechanical properties presented in Fig. 10 were randomly distributed to the same lattice mesh, which means that each value of modulus/strength is simply randomly assigned to a lattice element in the mesh. This way, the connectivity of phases is neglected. Note that elements having no strength/stiffness are kept at the same locations. In this way, a randomized microstructure was formed and its fracture performance under uniaxial tension was computed and compared with the results considering the “realistic” microstructure. The simulated stress-strain curve and its corresponding micromechanical properties are presented in Fig. 14 and Table 2. It is observed that the two cases have similar stiffness with difference in a range of 5%, because the input micromechanical properties have the same PDF. Unlike the elastic modulus of composite materials that is influenced by the properties of material components and their relative amounts, the (fracture) strength is governed by the weakest link in the system. Furthermore, the connectivity of weak phases (or pores) is present in the “real” system but is lost in the “random” system. As presented in Fig. 15, a completely different fracture pattern is observed. The main crack leading to the final failure shifts to the upper side. More distributed micro cracks are formed

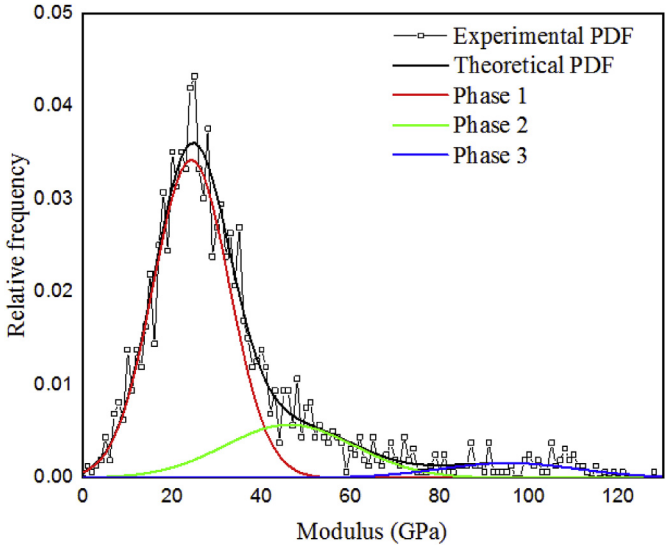

Fig. 16. Experimental and theoretical probability density function plots of Young's modulus from statistical indentation.

Table 3
Micromechanical properties of distinct solid phases determined by the deconvolution method and Eq. (5).

Phase name	Young's modulus (GPa)	Tensile strength (MPa)	Relative amount (%)
Outer hydration product	23.82	61.94	68.51
Inner hydration products	42.06	156.13	23.99
Anhydrous cement clinkers	90.30	540.78	7.5

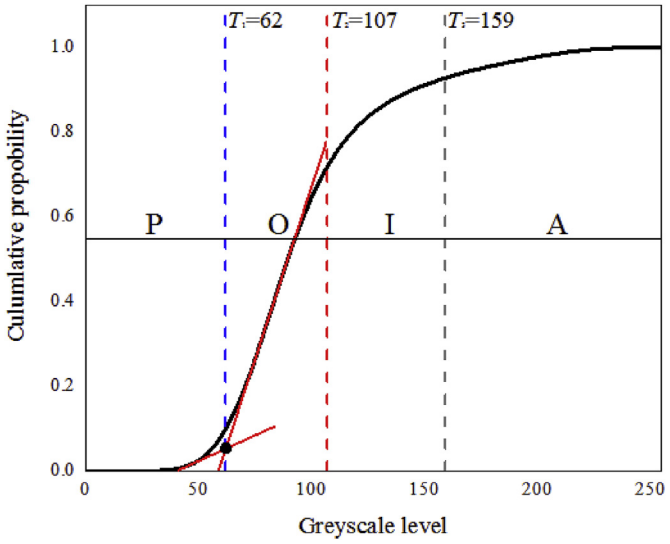

Fig. 17. Schematic view of threshold value determination.

before the localization and nucleation happen in the randomized microstructure. Therefore, as expected, the randomized microstructure has significantly higher strength, enables more deformation when reaches the peak load, and releases more fracture energy. Furthermore, it is worth mentioning that a sharper decrease occurs after reaching the peak load for the randomized microstructure, which is mainly attributed to the larger amount of pre-peak micro cracks compared to the "realistic" microstructure. On the other hand, for the "realistic"

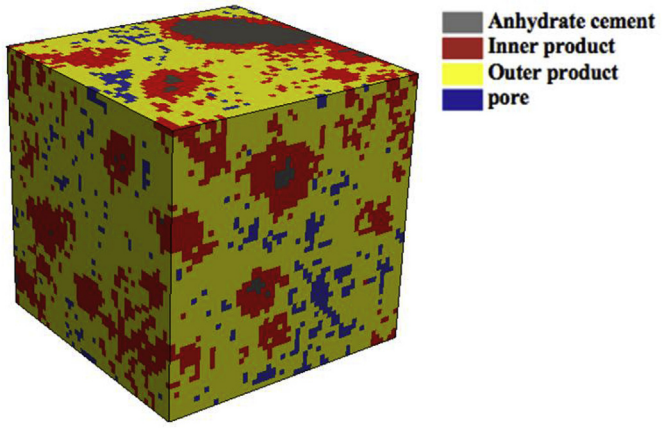

Fig. 18. 4-phase microstructure segmented from greyscale level based microstructure in Fig. 6.

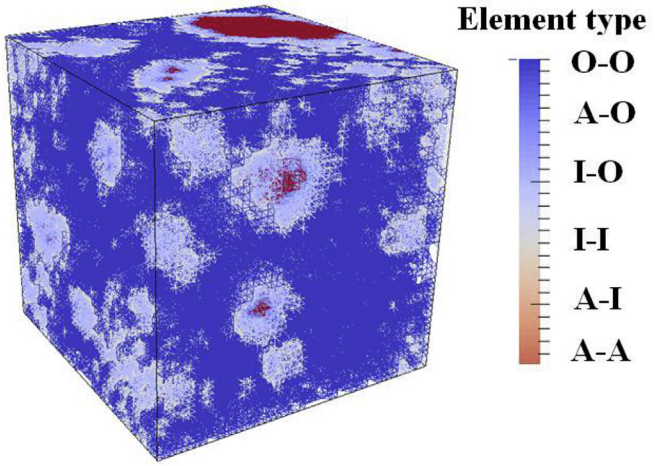

Fig. 19. Lattice discretization of 4-phase microstructure.

Table 4
Local mechanical properties of lattice elements.

Element type	Young's modulus (GPa)	Tensile strength (MPa)
A-A	90.30	540.78
A-I	57.89	156.13
A-O	37.70	61.94
I–I	42.06	156.13
I–O	30.42	61.94
O–O	23.82	61.94

microstructure, localized cracks develop around the "stiff inclusions" (mainly anhydrous clinker particles) after the initial cracking stage [33]. These cracks tend to interconnect more easily, but make more tortuous crack patterns, which enable more stable post-peak behaviour.

4.3. Comparison with method considering discrete phases

For comparison, the method considering discrete phases (4-phase method) was performed on the same material structure. The input micromechanical properties of induvial phases and their relative volume amount were derived from the statistical nanoindentation as shown in Fig. 16. This was achieved by a statistical deconvolution method consisting of fitting the experimental cumulative distribution of the measured modulus as described in Ref. [78]. It is assumed in this method that the distribution of each parameter is a combination of several Gaussian distributions, each corresponding to a different phase.

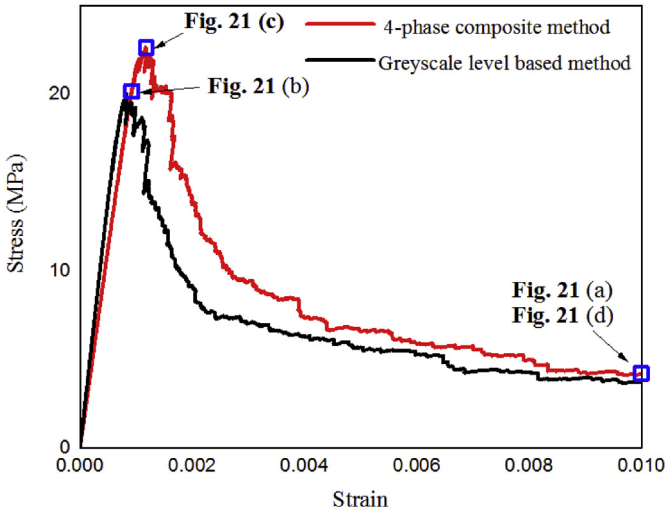

Fig. 20. Comparison of simulated stress-strain diagrams for greyscale level based microstructure and 4-phase microstructure (points for which crack patterns are displayed are marked).

Table 5
Simulated micromechanical properties of 4-phase composite microstructure.

Young's modulus (GPa)	Tensile strength (MPa)	Strain at peak load (%)	Fracture energy (J/m^2)
22.61	22.64	0.12	8.28

Three phases, namely outer hydration products (Phase 1), inner hydration products (Phase 2) and anhydrous cement clinkers (Phase 3) were determined and listed in Table 3. It is important to notice that these hydration products are averages overall all types of hydrates (including Portlandite, Ettringite, and Calcium Silicate Hydrates (C—S—H) of different mass densities) and small capillary pores. Although it is still under debate whether 3 phases should be distinguished from the statistical nanoindentation and what they indeed represent, again, the purpose of adopting this deconvolution method is to compare with the method using a continuous material structure proposed in this work. The distinction of two types of hydration products, inner and outer hydration products, is adopted here for simplification.

The elastic moduli of distinct phases (Table 3) determined in the current work are somewhat different from those reported results in the literature [17–19]. This is because the current results are derived from a different indentation depth, which results in a different interaction volume. The next step is related with segmentation phases from the greyscale level based microstructure. For this purpose, the global threshold method was applied. The cumulative distribution of greyscale level was used to determine the threshold value (see Fig. 17). In the current work, the upper threshold value of capillary pore (P) was determined by the tangent-slope method [4,15,39] in which greyscale value at inflection point in the cumulative distribution curve is used. This point represents the critical point where a small increment in the threshold value will cause a sharp increase in the segmented volume fraction of pores. The threshold of the rest phases were set to meet their relative amount determined by statistical nanoindentation. The determined relative amount is 0.0949, 0.6184, 0.2128 and 0.0740 for capillary pores (P), outer hydration products (O), inner hydration products (I) and anhydrous cement clinkers (A) respectively. The four intervals are then formed, and the voxel's phase can be labelled according to the interval its greyscale level falls in. The segmented material structure and its corresponding lattice mesh are presented in Fig. 18 and Fig. 19 respectively. Note that elements connecting the voxel labelled as pore were eliminated from the mesh. Therefore, six types of elements with different mechanical properties were generated (Table 4).

As shown in Fig. 20, the simulated stress-strain curve of the 4-phase composite is compared with the results from greyscale level based microstructure. Although similar stress-strain response is found for the two methods, the 4-phase composite has a somewhat lower stiffness but higher strength and fracture energy (Table 5). The lower stiffness is mainly attributed to the higher porosity included in the material [74], while the higher strength is because of the big difference between assigned mechanical properties. For example, the anhydrous cement particle works as the stiff inclusion in the matrix, forcing the crack to propagate around it. This results in a more tortuous and overlapped crack pattern. Thus, a more stable crack propagation and higher strength can be expected [39]. The higher porosity in the 4-phase method reduces the number of elements in the lattice system, which makes the main crack forms with less cracked elements, as more pre-existing defects can be localized or nucleated to form to the main crack. Fig. 21 shows the cracked 4-phase composite at final stage and the crack patterns at certain deformation levels. Although it is observed that the crack patterns at pre-peak stage are different for these two methods because of the difference in the pre-existing defects spatial distribution, the final crack patterns at final stage are almost identical to each other. This indicates that, on one hand, the pre-peak crack propagation is mainly governed by pre-existing defects, one the hand the stiff inclusions have more influence on the post-peak crack propagation and localization. This is in accordance with expectations: the pre-peak phase is characterised by microcrack growth, which is influenced by the defects, while the post peak phase is characterised by bridging and branching, which are influenced by the inclusions.

4.4. General discussion

As shown in the comparison, a similar fracture pattern and stress-strain response is found in between the 4-phase method and greyscale level based method. It is difficult to determine which method gives more satisfactory results on the micromechanical modelling, but the proposed approach is more generic and direct. It requires less processing steps (no need for deconvolution or averaging of properties, which might introduce errors) and can be always applied once the link is made between the greyscale value and the micromechanical properties. As the intrinsic heterogeneity of cement paste is directly implemented from the XCT scanning, no additional assumptions need to be made with regard to distribution of local micromechanical properties. The 4-phase method distinguishes four homogeneous phases with distinct material properties (no gradients are considered due to deconvolution and averaging); in reality, none of the phases considered is completely homogeneous, and a gradient of material properties in each of the phases might exist. This is probably captured better with the current model. With respect to the application, the grey-scale based method requires less prior knowledge, as no processing of the XCT images and the measured micromechanical properties is required. Therefore, the greyscale level based method shows advantages in micromechanical modelling of a composite material with limited knowledge on the microstructure and micromechanical properties of its constituents. However, it should be noted that the local micromechanical properties should be the representative of the XCT resolution. This is because, with resolution variation, different amounts of capillary porosity or defects may be included in a voxel thereby introducing different micromechanical properties of the voxel. Therefore, when this method is applied, the interaction volume probed by the nanoindenter must be kept the same as the image voxel size. It is worth mentioning that this issue should also be considered when using the 4-phase method. Furthermore, it is possible to improve the spatial resolution of current microstructure to 0.5 μm by XCT scanning without changing the scanned size of the specimen [39], or to 50 nm resolution with different setting [79,80]. But, again, the corresponding micromechanical

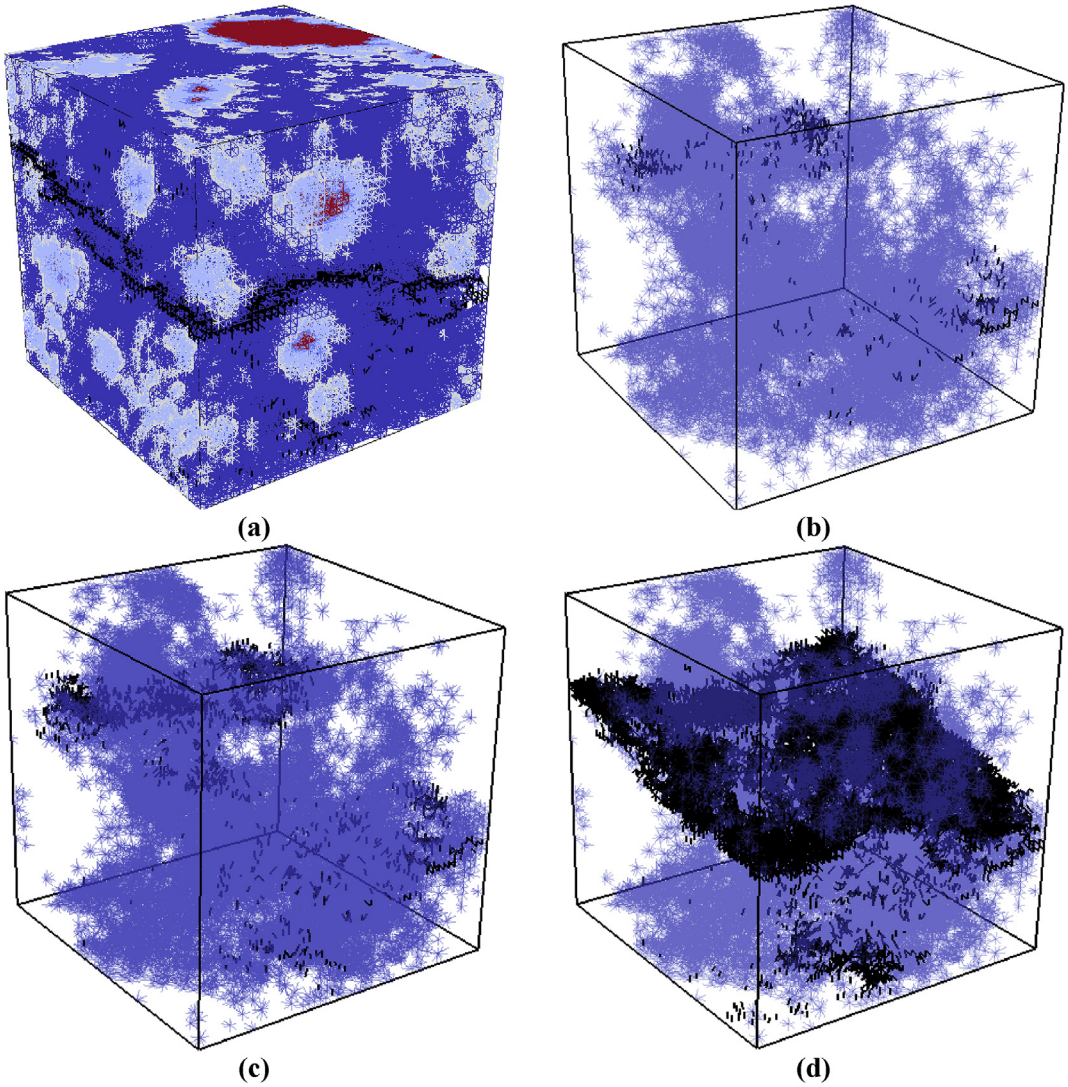

Fig. 21. Simulated fracture pattern of the 4-phase composite: **(a)** deformed specimen with cracked elements at the final stage with a strain of 0.01; **(b)** crack pattern at initial stage with 500 elements cracked; **(c)** crack pattern at peak load with 1848 cracked elements; **(d)** crack pattern at the final stage with 23917 cracked elements (black represents cracked element; blue elements in the crack pattern represent elements having no mechanical properties which are considered as the pre-existing defects in the simulation). (For interpretation of the references to colour in this figure legend, the reader is referred to the Web version of this article.)

properties should be determined from a smaller interaction volume. This can be achieved by deriving data from a shallower depth of nanoindentation test or using other techniques such as atomic force microscopy [81]. Furthermore, current limitations of the proposed method should be addressed. As we focus on the feasibility of the proposed continuous method, the relationship between the greyscale level and local mechanical properties was determined by assumption and statistical analysis. Although a validation procedure was carried out to prove the correctness of the assumption, a physical explanation is still lacking. Therefore, a throughout understanding of the relationship between the greyscale level and local mechanical properties is expected to be gained in the future to achieve the automatic assignment of local micromechanical properties from CT data for the micromechanical modelling.

5. Conclusions

In this work, a new approach for micromechanical modelling of cement paste is proposed. Without the need for explicit identification of distinct phases, the intrinsic heterogeneity of cement paste is directly implemented using original greyscale images obtained by XCT. The PDFs (i.e. histograms) of nanoindentation measurements (both Young's modulus and microhardness) and greyscale value were normalized linearly and tested by a two-sample K—S statistics, showing that a strong linear relationship exists between Young's modulus and greyscale level, while microhardness has a weak linear correlation with grayscale value. An empirical model in a form of power exponent was therefore proposed to correlate the hardness with its corresponding Young's modulus and showed a good fit. The micromechanical properties (E modulus and micro hardness) were then mapped to the voxels according to their greyscale level.

The deformation and fracture of a greyscale level based microstructure was simulated using a discrete lattice model. The influence of material heterogeneity and phase distribution on the mechanical performance is studied by comparing a “realistic” and a “randomized” microstructure. Although similar elastic moduli are obtained, much higher strength and more distributed micro cracks are observed in the “randomized” microstructure. Therefore, the distribution of heterogeneous phases in a composite quasi-brittle material like cement paste is critical when it comes to the overall mechanical behaviour. Phase connectivity plays an important role in the process of crack propagation and growth. If the phases are clustered in stiff and strong particles and

weak interfaces, it will lead to a much lower strength of the composite than in the case the same properties are randomly distributed over the sample. This leads to strong limitations when use of RVE and homogenization are considered for composites with crack localization.

The fracture behaviour of greyscale level based microstructure is also compared with the method considering discrete phases. The comparison shows that the strength of material obtained by the method considering discrete phases is higher compared to the method of greyscale level based microstructure. This might be attributed to the additional processing steps that are applied in the method considering discrete phases: deconvolution and averaging. Errors and biases might occur in any of these steps.

The proposed method is promising, because it captures the gradient of material properties in cement paste that is more realistic. However, a physical understanding behind the relationship between the CT data and local micromechanical properties is still not sufficiently understood and deserves further study. It is expected that, in the future, the fracture behaviour of different types of binders at the microscale possibly can be studied based only on XCT and the reliable link between the greyscale value obtained by XCT and micromechanical properties measured by nanoindentation as proposed in this study.

Acknowledgments

This work is supported in part by the scholarship from China Scholarship Council (CSC) [grant number 201506120067]. The authors would also like to acknowledge the help of Mr. Arjan Thijssen with the XCT experiment.

Appendix A. Supplementary data

Supplementary data related to this article can be found at https://doi.org/10.1016/j.compositesb.2018.08.102.

References

[1] Van Breugel K. Numerical simulation of hydration and microstructural development in hardening cement-based materials:(II) applications. Cement Concr Res 1995;25(3):522–30.
[2] Bishnoi S, Scrivener KL. μic: a new platform for modelling the hydration of cements. Cement Concr Res 2009;39(4):266–74.
[3] Bentz DP, Bentz DP. CEMHYD3D: a three-dimensional cement hydration and microstructure development modelling package. US Department of Commerce, National Institute of Standards and Technology; 2000Version 2.0.
[4] Scrivener KL. Backscattered electron imaging of cementitious microstructures: understanding and quantification. Cement Concr Compos 2004;26(8):935–45.
[5] Hall C, Colston SL, Jupe AC, Jacques SD, Livingston R, Ramadan AO, et al. Non-destructive tomographic energy-dispersive diffraction imaging of the interior of bulk concrete. Cement Concr Res 2000;30(3):491–5.
[6] Gallucci E, Scrivener K, Groso A, Stampanoni M, Margaritondo G. 3D experimental investigation of the microstructure of cement pastes using synchrotron X-ray microtomography (μCT). Cement Concr Res 2007;37(3):360–8.
[7] Chotard T, Boncoeur-Martel M, Smith A, Dupuy J, Gault C. Application of X-ray computed tomography to characterise the early hydration of calcium aluminate cement. Cement Concr Compos 2003;25(1):145–52.
[8] Bullard JW, Garboczi EJ. A model investigation of the influence of particle shape on portland cement hydration. Cement Concr Res 2006;36(6):1007–15.
[9] Liu C, Huang R, Zhang Y, Liu Z, Zhang M. Modelling of irregular-shaped cement particles and microstructural development of Portland cement. Construct Build Mater 2018;168:362–78.
[10] Pichler B, Hellmich C, Eberhardsteiner J. Spherical and acicular representation of hydrates in a micromechanical model for cement paste: prediction of early-age elasticity and strength. AcMec 2009;203(3):137–62.
[11] Zhang H, Šavija B, Schlangen E. Towards understanding stochastic fracture performance of cement paste at micro length scale based on numerical simulation. Construct Build Mater 2018;183:189–201.
[12] Promentilla MAB, Sugiyama T, Hitomi T, Takeda N. Quantification of tortuosity in hardened cement pastes using synchrotron-based X-ray computed microtomography. Cement Concr Res 2009;39(6):548–57.
[13] Zhang M, He Y, Ye G, Lange DA, van Breugel K. Computational investigation on mass diffusivity in Portland cement paste based on X-ray computed microtomography (μCT) image. Construct Build Mater 2012;27(1):472–81.
[14] Landis EN, Keane DT. X-ray microtomography. Mater Char 2010;61(12):1305–16.
[15] Zhang M, Jivkov AP. Micromechanical modelling of deformation and fracture of hydrating cement paste using X-ray computed tomography characterisation. Compos B Eng 2016;88:64–72.
[16] Han T-S, Zhang X, Kim J-S, Chung S-Y, Lim J-H, Linder C. Area of lineal-path function for describing the pore microstructures of cement paste and their relations to the mechanical properties simulated from μ-CT microstructures. Cement Concr Compos 2018;89:1–17.
[17] Hu C, Gao Y, Zhang Y, Li Z. Statistical nanoindentation technique in application to hardened cement pastes: influences of material microstructure and analysis method. Construct Build Mater 2016;113:306–16.
[18] Constantinides G, Ulm F-J. The effect of two types of CSH on the elasticity of cement-based materials: results from nanoindentation and micromechanical modeling. Cement Concr Res 2004;34(1):67–80.
[19] Velez K, Maximilien S, Damidot D, Fantozzi G, Sorrentino F. Determination by nanoindentation of elastic modulus and hardness of pure constituents of Portland cement clinker. Cement Concr Res 2001;31(4):555–61.
[20] Constantinides G, Ulm F-J, Van Vliet K. On the use of nanoindentation for cementitious materials. Mater Struct 2003;36(3):191–6.
[21] Manzano H, Dolado J, Guerrero A, Ayuela A. Mechanical properties of crystalline calcium-silicate-hydrates: comparison with cementitious C-S-H gels. Phys Status Solidi 2007;204(6):1775–80.
[22] Manzano H, Dolado JS, Ayuela A. Structural, mechanical, and reactivity properties of tricalcium aluminate using first-principles calculations. J Am Ceram Soc 2009;92(4):897–902.
[23] Zhang H, Šavija B, Figueiredo SC, Schlangen E. Experimentally validated multi-scale modelling scheme of deformation and fracture of cement paste. Cement Concr Res 2017;102:175–86.
[24] Lura P, Trtik P, Münch B. Validity of recent approaches for statistical nanoindentation of cement pastes. Cement Concr Compos 2011;33(4):457–65.
[25] Davydov D, Jirásek M, Kopecký L. Critical aspects of nano-indentation technique in application to hardened cement paste. Cement Concr Res 2011;41(1):20–9.
[26] Pichler B, Hellmich C. Upscaling quasi-brittle strength of cement paste and mortar: a multi-scale engineering mechanics model. Cement Concr Res 2011;41(5):467–76.
[27] Sanahuja J, Dormieux L, Chanvillard G. Modelling elasticity of a hydrating cement paste. Cement Concr Res 2007;37(10):1427–39.
[28] Bernard O, Ulm F-J, Lemarchand E. A multiscale micromechanics-hydration model for the early-age elastic properties of cement-based materials. Cement Concr Res 2003;33(9):1293–309.
[29] Hu C, Li Z. Micromechanical investigation of Portland cement paste. Construct Build Mater 2014;71:44–52.
[30] Bittnar Z. Microstructure-based micromechanical prediction of elastic properties in hydrating cement paste. Cement Concr Res 2006;36(9):1708–18.
[31] Ulm F-J, Vandamme M, Jennings HM, Vanzo J, Bentivegna M, Krakowiak KJ, et al. Does microstructure matter for statistical nanoindentation techniques? Cement Concr Compos 2010;32(1):92–9.
[32] Trtik P, Münch B, Lura P. A critical examination of statistical nanoindentation on model materials and hardened cement pastes based on virtual experiments. Cement Concr Compos 2009;31(10):705–14.
[33] Luković M, Schlangen E, Ye G. Combined experimental and numerical study of fracture behaviour of cement paste at the microlevel. Cement Concr Res 2015;73:123–35.
[34] Muller AC, Scrivener KL, Gajewicz AM, McDonald PJ. Densification of C–S–H measured by 1H NMR relaxometry. J Phys Chem C 2012;117(1):403–12.
[35] Königsberger M, Hellmich C, Pichler B. Densification of CSH is mainly driven by available precipitation space, as quantified through an analytical cement hydration model based on NMR data. Cement Concr Res 2016;88:170–83.
[36] Tennis PD, Jennings HM. A model for two types of calcium silicate hydrate in the microstructure of Portland cement pastes. Cement Concr Res 2000;30(6):855–63.
[37] Jennings HM. Refinements to colloid model of CSH in cement: CM-II. Cement Concr Res 2008;38(3):275–89.
[38] Zhang J, Scherer GW. Comparison of methods for arresting hydration of cement. Cement Concr Res 2011;41(10):1024–36.
[39] Zhang H, Šavija B, Chaves Figueiredo S, Lukovic M, Schlangen E. Microscale testing and modelling of cement paste as basis for multi-scale modelling. Materials 2016;9(11):907.
[40] Oliver WC, Pharr GM. An improved technique for determining hardness and elastic modulus using load and displacement sensing indentation experiments. J Mater Res 1992;7(6):1564–83.
[41] Bückle H. Use of the hardness test to determine other material properties. The Science of Hardness Testing and its Research Applications. 1973. p. 453.
[42] Chen JJ, Sorelli L, Vandamme M, Ulm FJ, Chanvillard G. A coupled nanoindentation/SEM-EDS study on low water/cement ratio portland cement paste: evidence for C–S–H/Ca (OH) 2 nanocomposites. J Am Ceram Soc 2010;93(5):1484–93.
[43] Vanzo J. A nanochemomechanical investigation of carbonated cement paste. Massachusetts Institute of Technology; 2009.
[44] Krakowiak KJ, Thomas JJ, Musso S, James S, Akono A-T, Ulm F-J. Nano-chemo-mechanical signature of conventional oil-well cement systems: effects of elevated temperature and curing time. Cement Concr Res 2015;67:103–21.
[45] Deirieh A, Ortega J, Ulm F-J, Abousleiman Y. Nanochemomechanical assessment of shale: a coupled WDS-indentation analysis. Acta Geotechnica 2012;7(4):271–95.
[46] Phillips D, Lannutti J. Measuring physical density with X-ray computed tomography. NDT E Int 1997;30(6):339–50.
[47] Jussiani EI, Appoloni CR. Effective atomic number and density determination of rocks by X-ray microtomography. Micron 2015;70:1–6.
[48] Sinka I, Burch S, Tweed J, Cunningham J. Measurement of density variations in tablets using X-ray computed tomography. Int J Pharm 2004;271(1–2):215–24.
[49] Kariem H, Hellmich C, Kiefer T, Jäger A, Füssl J. Micro-CT-based identification of double porosity in fired clay ceramics. J Mater Sci 2018;53(13):9411–28.

[50] Blanchard R, Morin C, Malandrino A, Vella A, Sant Z, Hellmich C. Patient-specific fracture risk assessment of vertebrae: a multiscale approach coupling X-ray physics and continuum micromechanics. International journal for numerical methods in biomedical engineering 2016;32(9).
[51] Gitman I, Askes H, Sluys L. Representative volume: existence and size determination. Eng Fract Mech 2007;74(16):2518–34.
[52] Douarche N, Rouby D, Peix G, Jouin J. Relations between X-ray tomography, density and mechanical properties in carbon–carbon composites. Carbon 2001;39(10):1455–65.
[53] Rho J, Hobatho M, Ashman R. Relations of mechanical properties to density and CT numbers in human bone. Med Eng Phys 1995;17(5):347–55.
[54] Edidin A, Taylor D, Bartel D. Automatic assignment of bone moduli from CT data: a 3-D finite element study. Trans Annu Meet Orthop Res Soc 1991;16:491.
[55] Keyak J, Meagher J, Skinner H, Mote Jr. C. Automated three-dimensional finite element modelling of bone: a new method. J Biomed Eng 1990;12(5):389–97.
[56] Shapurian T, Damoulis PD, Reiser GM, Griffin TJ, Rand WM. Quantitative evaluation of bone density using the Hounsfield index. Int J Oral Maxillofac Implants 2006;21(2).
[57] Massey Jr. FJ. The Kolmogorov-Smirnov test for goodness of fit. J Amer Statistical Assoc 1951;46(253):68–78.
[58] Cao R, Van Keilegom I. Empirical likelihood tests for two-sample problems via nonparametric density estimation. Can J Stat 2006;34(1):61–77.
[59] Gail MH, Green SB. Critical values for the one-sided two-sample Kolmogorov-Smirnov statistic. J Amer Statistical Assoc 1976;71(355):757–60.
[60] Day A, Snyder K, Garboczi E, Thorpe M. The elastic moduli of a sheet containing circular holes. J Mech Phys Solid 1992;40(5):1031–51.
[61] Zhang P, Li S, Zhang Z. General relationship between strength and hardness. Mater Sci Eng, A 2011;529:62–73.
[62] Schlangen E, Qian Z. 3D modeling of fracture in cement-based materials. J Multiscale Model (JMM) 2009;1(02):245–61.
[63] Šavija B, Pacheco J, Schlangen E. Lattice modeling of chloride diffusion in sound and cracked concrete. Cement Concr Compos 2013;42:30–40.
[64] Schlangen E. Experimental and numerical analysis of fracture processes in concrete PhD. Thesis Delft, The Netherlands: Delft University of Technology; 1993.
[65] Nikolić M, Karavelić E, Ibrahimbegovic A, Miščević P. Lattice element models and their peculiarities. Arch Comput Meth Eng 2017:1–32.
[66] Pan Z, Ma R, Wang D, Chen A. A review of lattice type model in fracture mechanics: theory, applications, and perspectives. Eng Fract Mech 2018;190:382–409.
[67] Šavija B, Liu D, Smith G, Hallam KR, Schlangen E, Flewitt PE. Experimentally informed multi-scale modelling of mechanical properties of quasi-brittle nuclear graphite. Eng Fract Mech 2016;153:360–77.
[68] Schlangen E, Garboczi E. Fracture simulations of concrete using lattice models: computational aspects. Eng Fract Mech 1997;57(2):319–32.
[69] Yip M, Mohle J, Bolander J. Automated modeling of three-dimensional structural components using irregular lattices. Comput Aided Civ Infrastruct Eng 2005;20(6):393–407.
[70] Mehta PK, Monteiro PJ. Microstructure and properties of hardened concrete. Concrete: Microstructure, properties and materials 2006:41–80.
[71] Qian Z, Schlangen E, Ye G, van Breugel K. Modeling framework for fracture in multiscale cement-based material structures. Materials 2017;10(6):587.
[72] Qian Z, Schlangen E, Ye G, Van Breugel K. Prediction of mechanical properties of cement paste at microscale. Mater Construcción 2010;60(297):7–18.
[73] Zhang H, Šavija B, Schlangen E. Combined experimental and numerical study on micro-cube indentation splitting test of cement paste. Eng Fract Mech 2018.https://doi.org/10.1016/j.engfracmech.2018.04.018. in press.
[74] Liu D, Šavija B, Smith GE, Flewitt PE, Lowe T, Schlangen E. Towards understanding the influence of porosity on mechanical and fracture behaviour of quasi-brittle materials: experiments and modelling. Int J Fract 2017:1–16.
[75] Liu D, Mingard K, Lord OT, Flewitt P. On the damage and fracture of nuclear graphite at multiple length-scales. JNuM 2017;493:246–54.
[76] Haecker C-J, Garboczi E, Bullard J, Bohn R, Sun Z, Shah S, et al. Modeling the linear elastic properties of Portland cement paste. Cement Concr Res 2005;35(10):1948–60.
[77] Luković M, Šavija B, Dong H, Schlangen E, Ye G. Micromechanical study of the interface properties in concrete repair systems. J Adv Concr Technol 2014;12(9):320–39.
[78] Miller M, Bobko C, Vandamme M, Ulm F-J. Surface roughness criteria for cement paste nanoindentation. Cement Concr Res 2008;38(4):467–76.
[79] Le Gros MA, McDermott G, Larabell CA. X-ray tomography of whole cells. Curr Opin Struct Biol 2005;15(5):593–600.
[80] Trtik P, Diaz A, Guizar-Sicairos M, Menzel A, Bunk O. Density mapping of hardened cement paste using ptychographic X-ray computed tomography. Cement Concr Compos 2013;36:71–7.
[81] Trtik P, Kaufmann J, Volz U. On the use of peak-force tapping atomic force microscopy for quantification of the local elastic modulus in hardened cement paste. Cement Concr Res 2012;42(1):215–21.